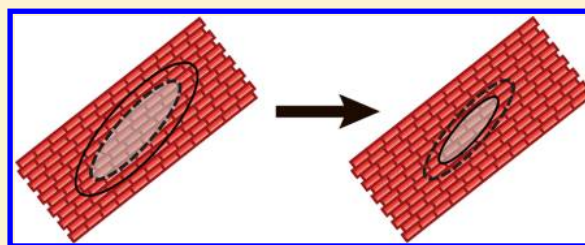


Thermally-Limited Exciton Delocalization in Superradiant Molecular Aggregates

Dylan H. Arias,[†] Katherine W. Stone,[‡] Sebastiaan M. Vlaming,[†] Brian J. Walker,^{†, §} Mounqi G. Bawendi,[†] Robert J. Silbey,^{†,||} Vladimir Bulović,[‡] and Keith A. Nelson^{*,†}

[†]Department of Chemistry and Center for Excitonics and [‡]Research Laboratory of Electronics and Center for Excitonics, Massachusetts Institute of Technology, Cambridge, Massachusetts 02139, United States

ABSTRACT: We present two-dimensional Fourier transform optical spectroscopy measurements of two types of molecular *J*-aggregate thin films and show that temperature-dependent dynamical effects govern exciton delocalization at all temperatures, even in the presence of significant inhomogeneity. Our results indicate that in the tested molecular aggregates, even when the static structure disorder dominates exciton dephasing dynamics, the extent of exciton delocalization may be limited by dynamical fluctuations, mainly exciton–phonon coupling. Thus inhomogeneous dephasing may mediate the exciton coherence time whereas dynamical fluctuations mediate the exciton coherence length.



INTRODUCTION

Naturally occurring light harvesting complexes are nanoscale systems optimized for light collection and energy transfer efficiency. Extensive study of these complexes has been aimed at understanding the underlying physical phenomena, including excitonic coherence and transport,^{1–5} that may be exploited for the development of new nanophotonic technologies. It has been of particular interest to fabricate and characterize thin films of molecular aggregates,⁶ as they may enable many of the features of light harvesting complexes to be adapted for selective applications and they may be integrated into active optoelectronic structures.^{7–9} Fabrication has recently been accomplished by forming thin films of *J*-aggregated polar molecules, a class of molecular aggregates that are related to natural antenna complexes and that are synthetically tractable.^{10,11} The optical responses of various *J*-aggregate morphologies are well correlated to specific synthesis routes, providing a method for tuning the excitonic properties of the aggregates for future applications.^{12–15} In *J*-aggregates, the number of molecules over which an exciton is delocalized mediates the linear and nonlinear optical responses such as absorption and superradiance^{16,17} as well as coherent and incoherent exciton transport.^{18–23} Several device architectures incorporating *J*-aggregate films take advantage of the excitons' enhanced optical responses.^{7,24–27} However, the relationships between exciton coherence and *J*-aggregate film morphology, structure, and environmental effects are not well understood. There are multiple mechanisms that limit exciton delocalization or coherence length N_{coh} (given in terms of the number of chromophores), including static disorder in the chromophore positions, energies, and orientations, and dynamic fluctuations caused primarily by exciton–phonon scattering.^{16,17,28–30} At low temperature T , exciton–phonon scattering should be infrequent and the delocalization could be limited to a value

$N_{\text{del}}^{\text{S}}$ due to static disorder, e.g., due to grain boundaries within the *J*-aggregated thin film (Figure 1a, left). At high T , exciton–phonon scattering will localize the exciton further (Figure 1a, right) to a dynamically limited length $N_{\text{del}}^{\text{D}}(T)$. In spectroscopic measurements, static disorder manifests as inhomogeneous dephasing and dynamic disorder as homogeneous dephasing, offering prospects for determination of the amount and type of disorder present in a system if the two types of dephasing can be distinguished.

Homogeneous and inhomogeneous dephasing are convolved in the line shapes obtained in one-dimensional linear optical spectra. We used two-dimensional Fourier transform optical (2D FTOPT) spectroscopy, which spreads spectral lines over two frequency axes, to separate the contributions to dephasing and to assess their effects on exciton delocalization. 2D FTOPT spectra were obtained for thin films of *J*-aggregating cyanine dyes and recorded over a range of temperatures. From the 2D spectra we extracted energy-dependent exciton coherence lengths by comparing ground-state and excited-state absorption frequencies whose difference depends on exciton size as discussed further below. Although exciton coherence dynamics have been investigated using 2D FTOPT spectroscopy in various nanostructured materials including *J*-aggregates,^{3–5,31–36} a systematic temperature-dependent study has not been reported that correlates energy-dependent exciton delocalization directly to both homogeneous and inhomogeneous dephasing.

In our 2D FTOPT measurements the first field, E_1 , excites exciton coherences and, after an “absorption” time delay τ_{abs}

Special Issue: Paul F. Barbara Memorial Issue

Received: August 31, 2012

Revised: November 28, 2012

Published: November 30, 2012

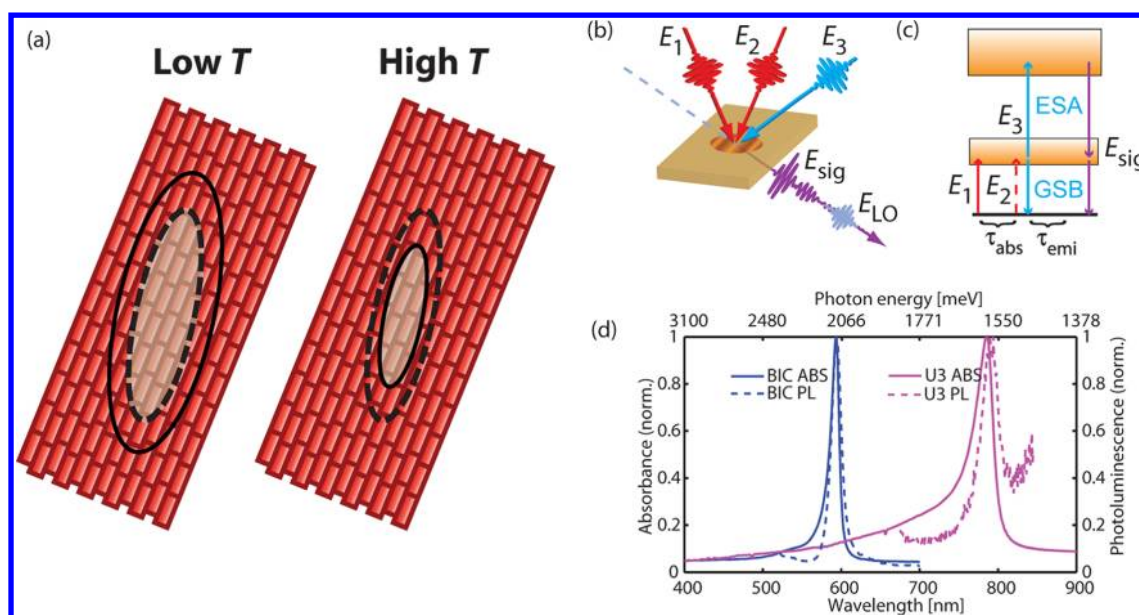


Figure 1. (a) Schematic illustration of *J*-aggregate molecular brickwork structure overlaid by pseudo-1D delocalized excitons (shaded in white). The dashed and solid ovals represent the exciton delocalization size limits imposed by static inhomogeneity (T -independent $N_{\text{del}}^{\text{d}}$) and by dynamic fluctuations ($N_{\text{del}}^{\text{d}}(T)$), respectively. In this illustration the exciton size N_{coh} is limited by $N_{\text{del}}^{\text{d}}$ at low T and $N_{\text{del}}^{\text{d}}(T)$ at high T . (b) Experimental geometry for 2D FTOPT spectroscopy of *J*-aggregate thin films. (c) Bands of one-exciton and two-exciton states and pulse interaction sequence for 2D FTOPT experiments, with the ground-state bleach (GSB) and excited-state absorption (ESA) signals indicated. (d) Room temperature linear absorption (ABS) and fluorescence (PL) for BIC and U3 *J*-aggregate thin films.

the second field, E_2 , generates a spatially varying grating pattern of exciton population. After a waiting time delay equivalent to the pump–probe delay time, the third field, E_3 , creates third-order coherences between the exciton state and either the ground state or higher lying, doubly excited states. After an “emission” time delay, τ_{emi} , the associated polarizations radiate the signal field, E_{sig} , superposed in the phase-matched direction with the reference field, E_{LO} , spectrally dispersed, and measured interferometrically to yield the complex signal. The (emission) frequency-resolved measurement is conducted as a function of the absorption time delay with respect to which Fourier transformation gives the 2D FTOPT spectrum whose peaks reveal the absorption and emission coherence frequencies.

With the time-ordering of femtosecond pulses illustrated in Figure 1b, we measure 2D rephasing or photon echo (PE) spectra whose line widths along the antidiagonal and diagonal frequency directions respectively yield the homogeneous and inhomogeneous dephasing rates.^{37,38} With the time-ordering of fields E_1 and E_2 reversed, we measure 2D nonrephasing spectra. Adding the rephasing and nonrephasing spectra, resulting in correlation spectra (CS), eliminates phase-twisted line shapes that appear in the 2D PE spectra due to mixing of absorptive and dispersive contributions to the nonlinear signal. The resulting line shapes can be interpreted as purely absorptive and dispersive signals.³⁹ The absorptive signal can be directly compared to a pump–probe spectrum where the frequency resolution of the pump is given by Fourier transform relationships while femtosecond time resolution is maintained. Like a pump–probe spectrum, a 2D CS can be used to obtain the exciton coherence size, N_{coh} .⁴⁰ However, a broad-band spectrally resolved pump–probe (SRPP) experiment will report only an averaged value because there is no selective excitation within the inhomogeneous exciton absorption spectrum.^{41,42} For a pump–probe experiment using narrow-band pulses, it is possible to determine both the absorption and emission

frequencies, and therefore which excitons are excited. However, narrow-band pulses are inherently long in time and if exciton relaxation occurs during the pulse it is no longer clear that the probed exciton is the same as the initially excited exciton. Using short pulses in 2D FTOPT spectroscopy circumvents this limitation by frequency resolving the excitation energy through Fourier transformation and resolving the emission via a spectrometer, resulting in both high time and frequency resolution.

EXPERIMENTAL DETAILS

The two *J*-aggregates studied were formed by cyanine dye molecules 1,1'-diethyl-3,3'-bis(sulfopropyl)-5,5',6,6'-tetrachlorobenzimidacarbocyanine (CAS No. 28272-54-0) and (3-[(2Z)-5-chloro-2-[(3E)-3-[5-chloro-3-(3-triethylammoniumsulfonatopropyl)-1,3-benzothiazol-3-ium-2-yl]methylene]-1,3-benzothiazol-3(2H)-yl]propane-1-sulfonate) (CAS No. 202135-09-9) (registry numbers supplied by author), which we refer to as BIC and U3, respectively. Both aggregates were deposited as thin film structures on sapphire substrates. BIC *J*-aggregates were formed via a layer-by-layer deposition method and consisted of 4.5 alternating layers, each 1.7 nm thick, of a cationic polymer and the anionic *J*-aggregating molecule to form a 7.7 nm thick film.⁶ U3 *J*-aggregates were prepared by spin-casting a thin film at 2000 rpm from a 2,2,2-trifluoroethanol solution (2 mg/mL) onto the substrate that had been cleaned as described previously.^{6,25} Atomic force micrographs indicated that the U3 film was 20 nm thick, with an RMS roughness of 0.8 nm. Sample deposition and preparation were performed in nitrogen atmosphere. Optical measurements were performed in a Janis ST100 coldfinger cryostat. For 2D FTOPT measurements on BIC *J*-aggregates, a Coherent Libra Ti:sapphire amplifier pumped a noncollinear parametric amplifier with 100 fs, 40 μJ pulses at 10 kHz to give pulses tuned to the absorption maximum of 595 nm and

compressed to 50 fs with a time-bandwidth product near 0.6 by a UV fused silica prism pair. A KMLabs Ti:sapphire oscillator with transform-limited 35 fs pulses at 92.5 MHz was tuned to an emission wavelength of 785 nm for measurements of the U3 *J*-aggregate film. In both experiments, the laser beam was focused to a 2D phase mask patterned to give efficient first-order diffraction at the appropriate wavelength. The four first-order diffracted beams composing the BOXCARs geometry were isolated and directed into a diffraction-based pulse shaper consisting of a grating and cylindrical lens that spectrally dispersed and focused the beams onto a 2D liquid crystal spatial light modulator (Hamamatsu X8267 for U3 experiments, Hamamatsu X7550 for BIC), giving full control of the spectral phase profile of each beam. This setup allowed control of optical delays and phases while maintaining full phase stability among the beams.^{31,32,43} About 100 pJ/pulse was used during all experiments to minimize exciton–exciton annihilation effects. We used a procedure outlined by Siemens et al.³⁸ to extract dephasing rates from the diagonal and antidiagonal line shapes of the 2D photon echo spectra.

THEORETICAL DESCRIPTION

Excitons in *J*-aggregating cyanine dyes are well described by the Frenkel model for interacting molecular excitations.^{28–30} The molecules can be assumed to be arranged in a one-dimensional chain, but it is straightforward to extend to higher dimensions as in the case of cylindrical aggregates.^{36,44–46} The exciton Hamiltonian is

$$H = \sum_{\mathbf{n}} \varepsilon_{\mathbf{n}} B_{\mathbf{n}}^{\dagger} B_{\mathbf{n}} + \sum_{\mathbf{m} \neq \mathbf{n}} J(\mathbf{m} - \mathbf{n}) B_{\mathbf{m}}^{\dagger} B_{\mathbf{n}} \quad (1)$$

The molecules are labeled by the index \mathbf{n} and $B_{\mathbf{n}}^{\dagger}$ creates an electronic excitation on molecule \mathbf{n} . The intermolecular coupling, $J(\mathbf{m} - \mathbf{n})$, is treated as dipole–dipole mediated transfer, thus $J(\mathbf{m} - \mathbf{n}) = -J/|\mathbf{m} - \mathbf{n}|^3$. Static disorder is introduced through a distribution of site energies, $\varepsilon_{\mathbf{n}}$, centered around the average site energy ε_0 . Diagonalization of the disordered exciton Hamiltonian yields exciton wave functions localized on sections of the aggregate. Dynamic disorder is typically introduced after diagonalization as exciton–phonon perturbations, leading to population relaxation and dephasing. Additionally, there are several energetically separated manifolds of states where each successive manifold consists of states with an additional excitation present. When the disorder is small compared to the intermolecular coupling, as in *J*-aggregates, the lowest energy states behave like those of a homogeneous aggregate delocalized over a reduced area of the full aggregate;^{47,48} these states resemble those of a particle confined in an infinite potential well. The lowest energy exciton state typically exhibits a wave function with no nodes, an S state; all the dipoles oscillate in phase, leading to superradiance.¹⁶ The next highest energy state delocalized over the same molecules often contains one node (a P state).⁴⁹ For a particle in an infinite potential well the energy difference between the S and P states reflects the size of the box. For a *J*-aggregate, this average energy difference, $\Delta = E_{\text{P}} - E_{\text{S}}$, reflects the average delocalization size of the exciton. The dominant optical transition from the one- to two-exciton manifold is typically from an S one-exciton state to an (approximately) SP-hybrid two-exciton state with the energy $E_{\text{P}} + E_{\text{S}}$. Third-order nonlinear spectroscopic techniques are interpreted using these lowest two manifolds of states, depicted in Figure 1c.

Spectrally resolved measurements are dominated by a ground-state bleach at the energy E_{S} corresponding to the ground state to S transition and by a blue-shifted excited-state absorption feature at the S to SP transition energy E_{P} . The difference in energy between these features is Δ .

The approximation that localized excitons retain properties similar to homogeneous, fully delocalized excitons is applicable to both one and two-dimensional *J*-aggregates.⁴⁴ Because we expect quasi-1D excitons in our system due to anisotropy in the intermolecular coupling, we analyze our results using a 1D model, noting that the trends we find would hold for either 1D or 2D systems (see Appendix for relationships for a 2D square lattice model). The exciton energy in a homogeneous linear *J*-aggregate restricted to nearest-neighbor coupling is $E_k = \varepsilon_0 - 2J \cos(\pi k/(N + 1))$, where ε_0 is the uncoupled excited-state energy, J is the coupling strength, N is the total number of molecules in the aggregate, and the integer k is used to denote the (unitless) wavevector $K = \pi k/(N + 1)$. Taking the energy difference between the P state ($k = 2$) and the S state ($k = 1$) and replacing the total number of molecules in the aggregate N with the effective coherence length N_{coh} leads to⁴⁰

$$N_{\text{coh}}(E_{\text{abs}}) = \pi \sqrt{\frac{3J}{\Delta(E_{\text{abs}})}} - 1 \quad (2)$$

In a 2D correlation spectrum, the absorption frequency is fully resolved, allowing us to deduce the delocalization length as a function of the S exciton absorption energy, E_{abs} (eq 2). A caveat is that the preceding interpretation of *J*-aggregate wave functions in terms of S and P states only holds in the low-energy tail of the density of states and that this picture does not hold for high-energy excitons.

The localization of the exciton wave function due to dynamical fluctuations and inhomogeneity leads to uncertainty in the exciton wavevector, and thus to uncertainty in the energy of the exciton. Expanding the homogeneous *J*-aggregate energy-wavevector dispersion relation above for small wavevectors K leads to a parabolic dispersion relation $E \approx \varepsilon_0 - 2J + JK^2$, similar to that of a quantum-mechanical particle in a box. The uncertainty in wavevector, δK , caused by localization gives rise to uncertainty in energy $\delta E \approx 2J(\delta K) + J(\delta K)^2$.³⁰ The exciton wavevector depends on the exciton coherence length, N_{coh} . The uncertainty in the exciton wavevector depends on exciton–phonon scattering and thus on the delocalization length given by dynamic disorder, $N_{\text{del}}^{\text{d}}$. There are two temperature regimes of interest, illustrated in Figure 1a. At low temperatures, associated with infrequent dynamic scattering events, static disorder dominates and the exciton momentum is a good quantum number such that $K \gg \delta K$. In this case $N_{\text{del}}^{\text{d}}$ plays no role because it is much longer than the temperature-independent delocalization length controlled by static disorder, $N_{\text{del}}^{\text{s}}$, i.e., $N_{\text{coh}} = N_{\text{del}}^{\text{s}}$. At higher temperatures, dynamic exciton scattering events lead to localization within a smaller size, i.e., $N_{\text{coh}} = N_{\text{del}}^{\text{d}} < N_{\text{del}}^{\text{s}}$. In the high-temperature limit, the exciton momentum is no longer a good quantum number because the fluctuations in K within any region are large, i.e., $\delta K \sim K$, and $\delta E \sim |J|/(N_{\text{coh}})^2$. Identifying the high- T energy uncertainty with the homogeneous line width of the exciton absorption spectrum, γ_{hom} , leads to

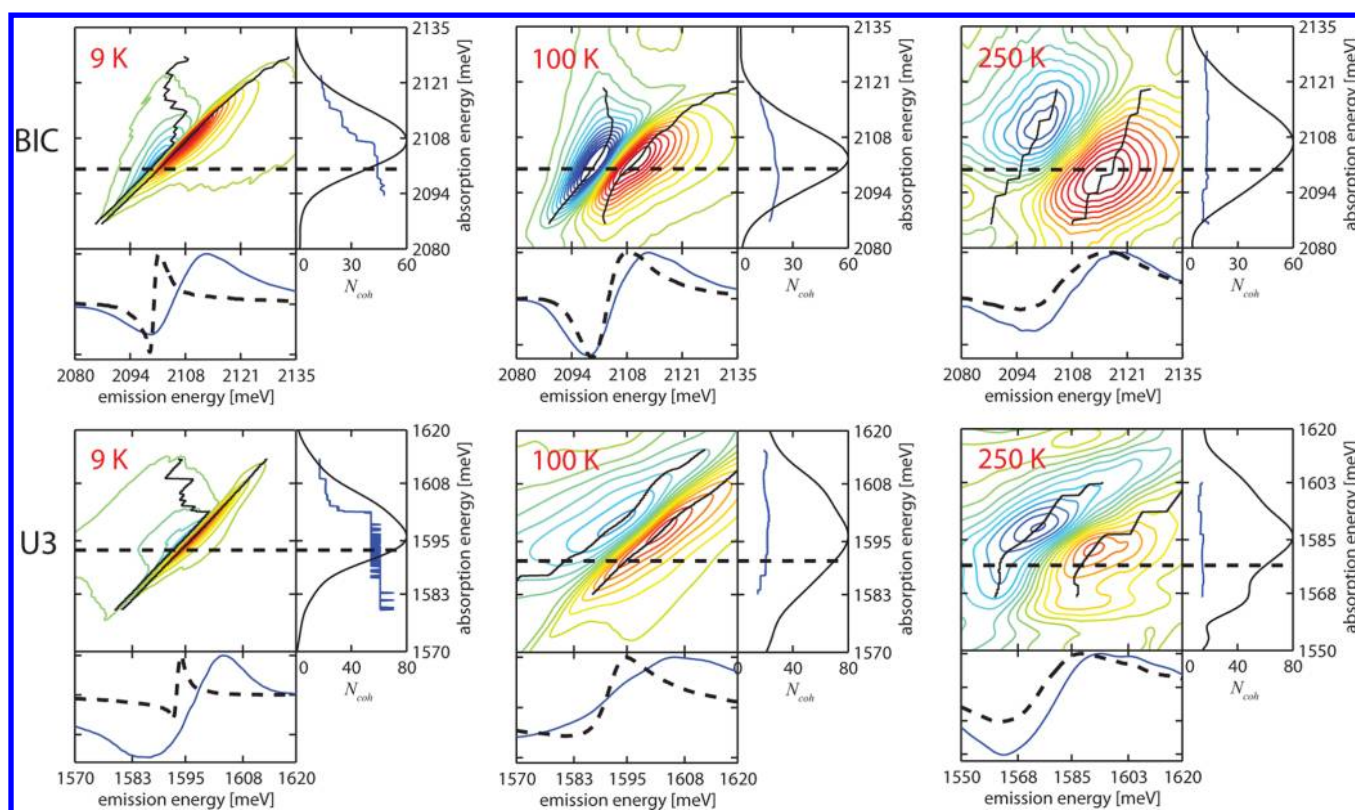


Figure 2. 2D CS for BIC (top row) and U3 (bottom row) *J*-aggregate thin films for several temperatures. Each panel presents a 2D CS with the ESA and GSB maxima as a function of energy shown, and based on the differences between them, $N_{\text{coh}}(E_{\text{abs}})$ indicated by the blue traces in the panels on the right. The heavy dashed lines indicate an exciton energy in the range used to determine the average value of N_{coh} at each T . The emission spectrum for this absorption energy is shown in the lower panel (black dashed line). Also shown are the signal projections to the emission energy axis (blue lines in lower panels) and the projection of the signal magnitude onto the absorption energy axis (black lines, right panels).

$$N_{\text{coh}} = \begin{cases} N_{\text{del}}^s & \text{low } T \\ N_{\text{del}}^d \propto \left(\frac{|J|}{\gamma_{\text{hom}}} \right)^{1/2} & \text{high } T \end{cases} \quad (3)$$

In the model, the exciton coherence length increases as the temperature is reduced until the static delocalization length is reached, at which point N_{coh} becomes T -independent.

RESULTS AND DISCUSSION

The thin film samples exhibited strong red-shifted and narrowed linear absorption spectra compared to the isolated dye molecules, archetypal signs of *J*-aggregation (Figure 1d). Representative 2D CS for BIC and U3 *J*-aggregate films at 9, 100, and 250 K with zero waiting time are shown in Figure 2. The spectra for BIC (top) and U3 (bottom) show similar features, with no spectra showing significant changes within the first few hundred femtoseconds of waiting time except for an overall lowering of the signal strength. The spectra blue-shifted and narrowed as temperature was decreased, similar to the temperature-dependent trends of other *J*-aggregates.³⁰ Each 2D correlation spectrum exhibits positive (red contours) and negative (blue contours) features resulting from excited-state absorption and ground-state bleach, respectively. Solid black lines on the 2D CS show the points of minimum and maximum signal used to determine the energy offset, Δ , from which the coherence length is calculated. The 1D model yielded nearest-neighbor intermolecular coupling constants of 153 meV for BIC and 212 meV for U3, estimated from the shift of the *J*-

aggregate absorption compared to the monomer.⁵⁰ Spectrally resolved pump–probe (SRPP) spectra in Figure 2 (lower panels, blue lines) are given by the projection of the 2D CS onto the emission energy axis. However, at low T , the SRPP do not reflect the narrow low-temperature homogeneous line widths. Instead, the peaks are broadened by the inhomogeneity of the films, thereby increasing the apparent separation between the bleach and excited-state absorption features and leading to an artificially decreased value for the exciton coherence length. Cuts of the 2D CS spectra at specific absorption energies (black dotted lines in Figure 2) demonstrate the narrow line widths for a single exciton energy. As the temperature increases and the total line shape becomes more homogeneous, the spectral features of excitons at different energies broaden until there is almost no difference between their line widths and those of the SRPP spectra. Using eq 2 for the 1D model we extracted the coherence lengths and then averaged around the red edge of the absorption peak to find a coherence length representative of the average exciton. The coherence length temperature dependences from 9 to 250 K for both *J*-aggregate films are shown in Figure 3. Contrary to the expectation of the model described above, we found that the coherence length decreases monotonically over the entire temperature range.

Temperature-dependent 2D PE spectra (Figure 4) of both U3 and BIC *J*-aggregates demonstrate the changing relative contributions of inhomogeneous and homogeneous broadening to the spectral line shapes. Using a fitting procedure,³⁸ we extracted the two dephasing rates for all temperatures. Figure 5 shows that for both *J*-aggregates, the inhomogeneous

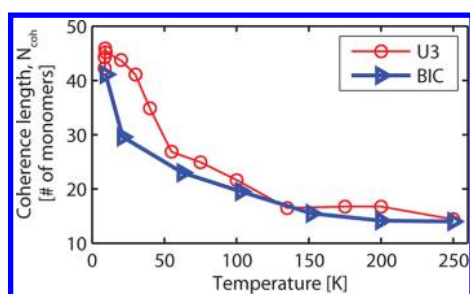


Figure 3. 1D model exciton coherence length as a function of temperature. The coherence length decreases monotonically for all T .

contributions are significantly larger than the homogeneous contributions at low T , whereas the rates become more comparable at higher T . The homogeneous line widths for both U3 and BIC scale linearly with temperature (Figure 5 (bottom)), which would be expected from dephasing through single-phonon interactions with a sublinear spectral density.^{51,52} Even though the inhomogeneous broadening σ is greater than the homogeneous broadening γ for most temperatures, N_{coh} tracks the homogeneous dephasing rate across all temperatures.

Fitting N_{coh} versus J/γ reveals that localization is controlled by dynamic scattering as described by eq 3 even down to temperatures as low as 9 K (Figure 6). According to eq 3, it is clear that as T is reduced the data show no transition from dynamic to static disorder-controlled delocalization length, as would be evidenced by a change in slope from -0.5 to 0 at low T where N_{coh} would become T -independent. The 2D

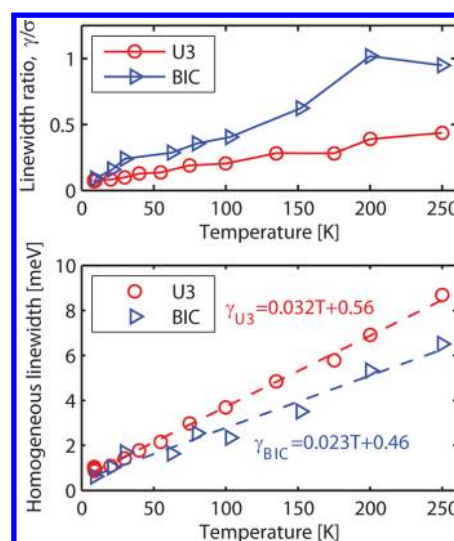


Figure 5. Homogeneous line width temperature dependence for BIC and U3 J-aggregates: (top) ratio of homogeneous line width (γ) to inhomogeneous line width (σ); (bottom) homogeneous line width versus T .

correlation spectra shown in Figure 2 and collected at other temperatures, which clearly show that the difference between ESA and GSB transition energies continuing to decrease with T even at the lowest temperatures, already make it clear that N_{coh} never reaches a T -independent value limited by inhomogeneity.

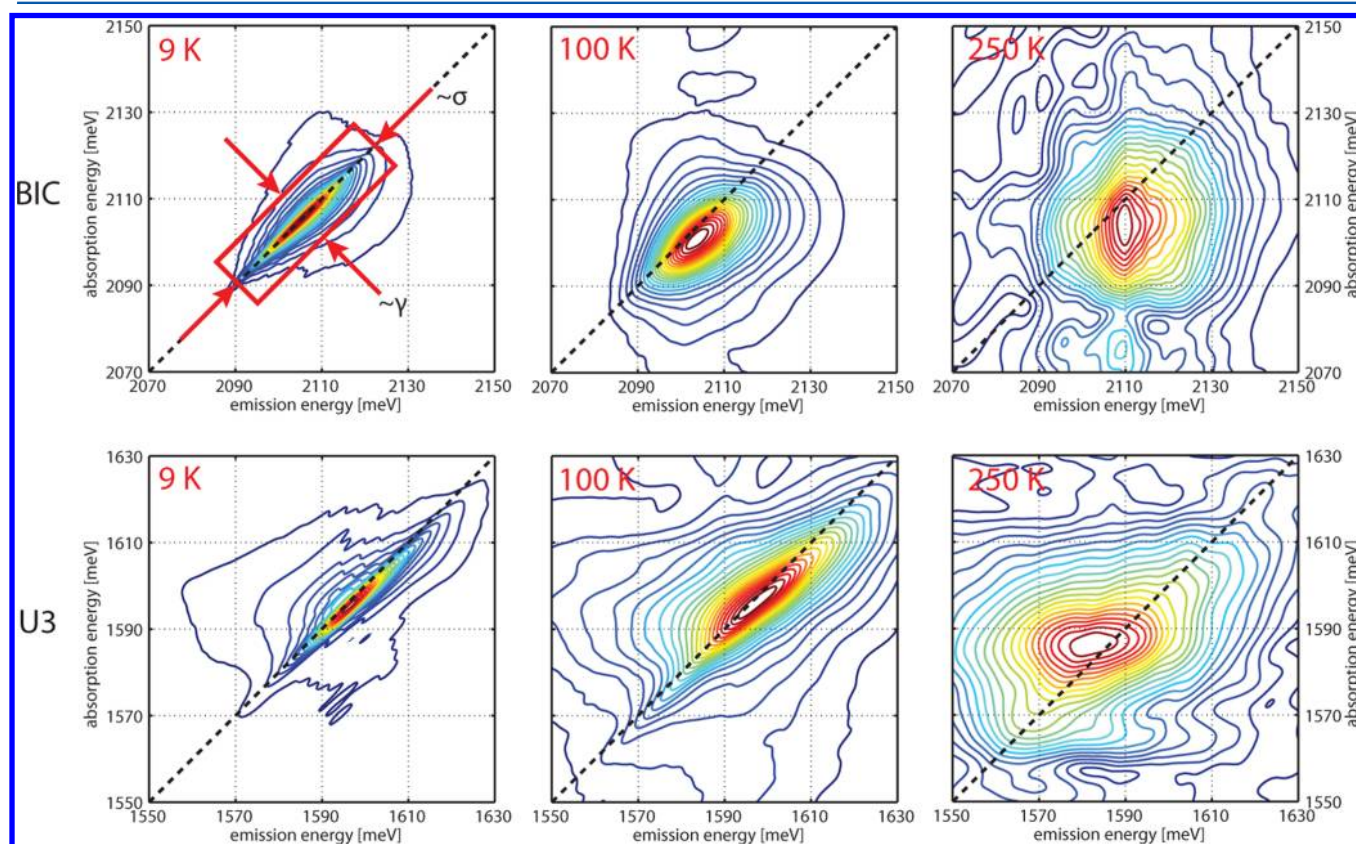


Figure 4. 2D PE spectra for BIC (top row) and U3 (bottom row) J-aggregates. The elongation along the diagonal indicates a large inhomogeneous dephasing rate, σ . The narrow anti-diagonal indicates a comparatively small homogeneous dephasing rate, γ . As the temperature increases from 9 K (left column) to 250 K (right column), the homogeneous dephasing rate increases, as evidenced by the increasing anti-diagonal line width.

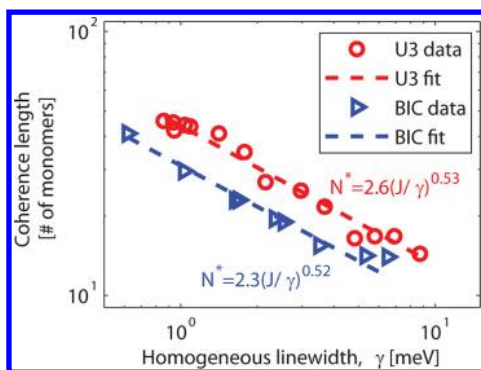


Figure 6. Log–log plot of coherence length versus homogeneous line width for BIC and U3 *J*-aggregates. The data throughout their ranges are fit well by the high temperature expression in eq 3, implying that dynamic disorder controls localization to temperatures as low as 9 K.

It is expected that the brickwork lattice has properties somewhere between the fully 1D and 2D cases due to anisotropic intermolecular coupling. The results shown in Figure 6 suggest primarily 1D exciton delocalization, but even a relatively small amount of interaction in a second dimension could significantly circumvent localization due to static inhomogeneity that is characteristic of purely 1D behavior.¹⁷ Thus 2D electronic interactions may play a role in the absence of static disorder-induced exciton localization even at the lowest temperatures.

CONCLUSIONS

In summary, we measured and compared homogeneous and inhomogeneous line widths and coherence lengths for two different nanostructured *J*-aggregate thin films using the unique capabilities of 2D FTOPT spectroscopy. We found that dynamic disorder dictates the coherent size of the excitons at all temperatures measured, down to 9 K, even in the presence of inhomogeneous dephasing that is an order of magnitude faster than the homogeneous dephasing. Thus dynamic disorder may control the exciton coherence length whereas static disorder controls the exciton coherence time. This is in contrast to previous reports that found a crossover temperature of ~ 40 K^{16,30} below which static disorder limited the exciton coherence size. Our results suggest that if synthetic systems such as *J*-aggregate films with selected morphologies can be engineered with controlled exciton–phonon coupling and dimensionality (i.e., anisotropy) of intermolecular electronic interactions, then the exciton coherence lengths may be increased accordingly, even in the presence of inhomogeneity.

APPENDIX

Extension to Two Dimensions

The Frenkel exciton analysis carried out in the main text for one dimension is easily extended to two dimensions. In the case of a rectangular lattice where each molecule lies on a grid of evenly spaced points in both dimensions with isotropic intermolecular coupling, the Hamiltonian is separable into two one-dimensional contributions, each identical to the one-dimensional Frenkel exciton Hamiltonian. This Hamiltonian becomes immediately solvable, with the wavefunctions

$$|k_1, k_2\rangle \propto \sum_{n,m} \sin \frac{\pi k_1 n}{L+1} \sin \frac{\pi k_2 m}{L+1} |n, m\rangle \quad (4)$$

with corresponding energies

$$E_{k_1 k_2} = \omega_0 - 2J \left(\cos \frac{\pi k_1}{L+1} + \cos \frac{\pi k_2}{L+1} \right) \quad (5)$$

Near the bottom of the band (small wavevector), we can make a Taylor expansion of the energies, giving

$$E_{k_1 k_2} = \omega_0 - 4J + \frac{\pi^2 J}{(L+1)^2} (k_1^2 + k_2^2) \quad (6)$$

The lowest energy state is the superradiant state with energy E_{11} , whereas the lowest energy two-exciton state is the state with energy E_{12} or E_{21} . The energy difference between these states, Δ , is determined in the 2D FTOPT experiments.

$$\Delta = \frac{3\pi^2 J}{(L+1)^2} \quad (7)$$

However, in the case of a 2D lattice, the number of molecules, N_{coh} , participating in the coherence now scales with L^2 and is proportional to an area. Thus, we write

$$N_{\text{coh}} \propto \left(\pi \sqrt{\frac{3J}{\Delta}} - 1 \right)^2 \quad (8)$$

To relate N_{coh} in 2D to the dynamic dephasing, we follow the same logic as before. Using $K^2 = k_1^2 + k_2^2$, we rewrite eq 6 as

$$E_K = \omega_0 - 4J + \frac{\pi^2 J}{(L+1)^2} K^2 \quad (9)$$

Allowing uncertainty in the momentum, $K \rightarrow K + \delta K$, gives $\delta E \approx J(2K(\delta K) + (\delta K)^2)$, as in the 1D case. Equating δE with γ_{hom} and taking the high T limit where localization is governed by dynamic disorder results in $N \propto 3J/\gamma_{\text{hom}}$.

Experimental Setup Details

The experimental procedures followed that of Turner et al.⁴³ Briefly, the laser beam first entered a beam shaper consisting of a 1:1 telescope around a two-dimensional binary phase mask pattern of 20 μm period. The four first-order diffraction spots were isolated and sent into a 4f-pulse shaper for diffraction-based pulse shaping. The beams were spectrally dispersed by diffraction from a grating (typically around 1000 lines/mm). The dispersed frequency components were focused by a cylindrical lens onto a two-dimensional spatial light modulator (SLM). Each dispersed beam occupied a different horizontal stripe of the SLM, where independent frequency-dependent phase patterns were applied to control the relative phases and temporal delays of the pulses in the beams. The longest delay in the experiments was 2.5 ps, well within the capabilities of the pulse shaper. Control over the phase of each spectral component in each dispersed beam was achieved by a sawtooth diffraction pattern in the vertical dimension of the SLM. The amplitude and phase of the first-order diffracted spot were controlled by the amplitude and spatial phase of the diffraction pattern. The first-order diffraction spots for all the beams were reflected by a pick-off mirror in the Fourier plane, isolated spatially, and collimated by the exit lens of the pulse shaper. The four beams were focused by a final 15 cm lens onto the sample, and the signal and reference beams were collected by another 15 cm lens and sent to a spectrometer. Due to the pixelated nature of the pulse shaping SLMs, there is a decrease of light intensity as a pulse is delayed.⁵³ This leads to a decrease in signal as a function of time delay, and thus to an apparent

increase in dephasing rate. However, the intensity roll-off is approximately exponential, allowing a simple correction for determination of the experimental dephasing rates.

AUTHOR INFORMATION

Corresponding Author

*E-mail: kanelson@mit.edu. Phone: (617) 253 1423. Fax: (617) 253 7030.

Present Address

[§]Cavendish Laboratory, University of Cambridge, Cambridge, UK CB30HE.

Notes

The authors declare no competing financial interest.

^{||}Author is deceased.

ACKNOWLEDGMENTS

This work was supported by the Center for Excitonics, an Energy Frontier Research Center funded by the U.S. Department of Energy, Office of Science, Office of Basic Energy Sciences under Award No. DE-SC0001088.

REFERENCES

- (1) Scholes, G.; Rumbles, G. *Nat. Mater.* **2006**, *5*, 683–696.
- (2) Scholes, G.; Fleming, G.; Olaya-Castro, A.; van Grondelle, R. *Nat. Chem.* **2011**, *3*, 763–774.
- (3) Collini, E.; Wong, C.; Wilk, K.; Curmi, P.; Brumer, P.; Scholes, G. *Nature* **2010**, *463*, 644–647.
- (4) Engel, G.; Calhoun, T.; Read, E.; Ahn, T.; Mančal, T.; Cheng, Y.; Blankenship, R.; Fleming, G. *Nature* **2007**, *446*, 782–786.
- (5) Brixner, T.; Stenger, J.; Vaswani, H.; Cho, M.; Blankenship, R.; Fleming, G. *Nature* **2005**, *434*, 625–8.
- (6) Bradley, M.; Tischler, J.; Bulović, V. *Adv. Mater.* **2005**, *17*, 1881–1886.
- (7) Tischler, J.; Bradley, M.; Bulović, V. *Phys. Rev. Lett.* **2005**, *95*, 036401.
- (8) Tischler, J.; Bradley, M.; Bulović, V. *Opt. Lett.* **2006**, *31*, 2045–7.
- (9) Akselrod, G.; Walker, B.; Tisdale, W.; Bawendi, M.; Bulović, V. *ACS Nano* **2012**, *6*, 467–71.
- (10) Jelley, E. *Nature* **1936**, *138*, 1009.
- (11) Kobayashi, T., Ed. *J-aggregates*; World Scientific: Singapore, 1996; pp 1–228.
- (12) Eisele, D.; Knoester, J.; Kirstein, S.; Rabe, J.; Vanden Bout, D. *Nat. Nanotechnol.* **2009**, *4*, 658–63.
- (13) Kirstein, S.; Daehne, S. *Int. J. Photoenergy* **2006**, *2006*, 1–21.
- (14) von Berlepsch, H.; Kirstein, S.; Böttcher, C. *J. Phys. Chem. B* **2003**, *107*, 9646–9654.
- (15) von Berlepsch, H.; Böttcher, C.; Quart, A.; Burger, C.; Dahne, S.; Kirstein, S. *J. Phys. Chem. B* **2000**, *104*, 5255–5262.
- (16) de Boer, S.; Wiersma, D. *Chem. Phys. Lett.* **1990**, *165*, 45–53.
- (17) Meier, T.; Chernyak, V.; Mukamel, S. *J. Phys. Chem. B* **1997**, *101*, 7332–7342.
- (18) Beljonne, D.; Curutchet, C.; Scholes, G.; Silbey, R. *J. Phys. Chem. B* **2009**, *113*, 6583–99.
- (19) Emelianova, E.; Athanasopoulos, S.; Silbey, R.; Beljonne, D. *Phys. Rev. Lett.* **2010**, *104*, 206405.
- (20) Athanasopoulos, S.; Emelianova, E.; Walker, A.; Beljonne, D. *Phys. Rev. B* **2009**, *80*, 195209.
- (21) Huijser, A.; Savenije, T.; Meskers, S.; Vermeulen, M.; Siebbeles, L. *J. Am. Chem. Soc.* **2008**, *130*, 12496–500.
- (22) Akselrod, G.; Tischler, Y.; Young, E.; Nocera, D.; Bulović, V. *Phys. Rev. B* **2010**, *82*, 113106.
- (23) Valteau, S.; Saikin, S.; Yung, M.; Aspuru-Guzik, A. *J. Chem. Phys.* **2012**, *137*, 034109.
- (24) Walker, B.; Dorn, A. *Nano Lett.* **2011**, *11*, 2655–2659.
- (25) Walker, B.; Bulović, V.; Bawendi, M. *Nano Lett.* **2010**, *10*, 3995–3999.
- (26) Wenus, J.; Ceccarelli, S.; Lidzey, D.; Tolmachev, A.; Slominskii, J.; Bricks, J. *Org. Electron.* **2007**, *8*, 120–126.
- (27) Scholes, G. *Chem. Phys.* **2002**, *275*, 373–386.
- (28) Spano, F.; Kuklinski, J.; Mukamel, S. *Phys. Rev. Lett.* **1990**, *65*, 211–214.
- (29) Bednarz, M.; Malyshev, V.; Knoester, J. *Phys. Rev. Lett.* **2003**, *91*, 217401.
- (30) Heijs, D.; Malyshev, V.; Knoester, J. *Phys. Rev. Lett.* **2005**, *95*, 177402.
- (31) Turner, D.; Nelson, K. *Nature* **2010**, *466*, 1089–1092.
- (32) Stone, K.; Gundogdu, K.; Turner, D.; Li, X.; Cundiff, S.; Nelson, K. *Science* **2009**, *324*, 1169–73.
- (33) Collini, E.; Scholes, G. *Science* **2009**, *323*, 369–73.
- (34) Stiopkin, I.; Brixner, T.; Yang, M.; Fleming, G. *J. Phys. Chem. B* **2006**, *110*, 20032–7.
- (35) Womick, J.; Miller, S.; Moran, A. *J. Phys. Chem. A* **2009**, *113*, 6587–98.
- (36) Sperling, J.; Nemeth, A.; Hauer, J.; Abramavicius, D.; Mukamel, S.; Kauffmann, H.; Milota, F. *J. Phys. Chem. A* **2010**, *114*, 8179–89.
- (37) Tokmakoff, A. *J. Phys. Chem. A* **2000**, *104*, 4247–4255.
- (38) Siemens, M.; Moody, G.; Li, H.; Bristow, A.; Cundiff, S. *Opt. Express* **2010**, *18*, 17699–708.
- (39) Khalil, M.; Demirdöven, N.; Tokmakoff, A. *Phys. Rev. Lett.* **2003**, *90*, 047401.
- (40) Dijkstra, A.; la Cour Jansen, T.; Knoester, J. *J. Chem. Phys.* **2008**, *128*, 164511.
- (41) Knoester, J. *J. Chem. Phys.* **1993**, *99*, 8466–8479.
- (42) Durrant, J.; Knoester, J.; Wiersma, D. *Chem. Phys. Lett.* **1994**, *222*, 450–456.
- (43) Turner, D.; Stone, K.; Gundogdu, K.; Nelson, K. *Rev. Sci. Instrum.* **2011**, *82*, 081301.
- (44) Didraga, C.; Knoester, J. *J. Chem. Phys.* **2004**, *121*, 946–59.
- (45) Didraga, C.; Pugzlys, A.; Hania, P.; von Berlepsch, H.; Duppen, K.; Knoester, J. *J. Phys. Chem. B* **2004**, *108*, 14976–14985.
- (46) Pugzlys, A.; Augulis, R.; Van Loosdrecht, P.; Didraga, C.; Malyshev, V.; Knoester, J. *J. Phys. Chem. B* **2006**, *110*, 20268–76.
- (47) Malyshev, V. *Opt. Spectrosc.* **1991**, *71*, 873–875.
- (48) Malyshev, V. *J. Lumin.* **1993**, *55*, 225–230.
- (49) Malyshev, V.; Moreno, P. *Phys. Rev. B* **1995**, *51*, 14587–14593.
- (50) Fidler, H.; Knoester, J.; Wiersma, D. *J. Chem. Phys.* **1991**, *95*, 7880.
- (51) Heijs, D.; Malyshev, V.; Knoester, J. *J. Chem. Phys.* **2005**, *123*, 144507.
- (52) Schultheis, L.; Honold, A.; Kuhl, J.; Köhler, K.; Tu, C. *Phys. Rev. B* **1986**, *34*, 9027.
- (53) Vaughan, J.; Feurer, T.; Stone, K.; Nelson, K. *Opt. Express* **2006**, *14*, 1314.